



The impact of rails on high-speed train slipstream and wake

Shibo Wang^{a,*}, David Burton^a, Astrid H. Herbst^b, John Sheridan^a, Mark C. Thompson^a

^a Fluids Laboratory for Aeronautical and Industrial Research (FLAIR), Dept. of Mechanical Engineering, Monash University, Australia

^b Centre of Competence for Aero- and Thermodynamics, Bombardier Transportation, Västerås, Sweden



ARTICLE INFO

Keywords:

High-speed trains
Train aerodynamics
Rails
Slipstream
Wake
Computational fluid dynamics (CFD)
Detached eddy simulation (DES)

ABSTRACT

Slipstream is the induced movement of air as a high-speed train (HST) passes. Previous studies have shown that the development of slipstream is highly geometry dependent, including both the geometries of the trains and nearby objects. Much effort has been channelled into reducing slipstream through optimisation of the train geometry; however, the impact of the rails on train aerodynamics remains largely unexplored. This study analyses the effect of rails on HST slipstream characteristics by systematically comparing the wakes for two geometric configurations incorporating: No Rails (NR) and With Rails (WR). The train model remains identical in both configurations, with the only difference being whether rails are included. This study highlights the potential effects of rails on HST slipstream characteristics, and reveals the underlying mechanism of how the rails shape the wake flow structures. By examining both mean and time-dependent flow features, the simulations show that the rails can significantly alter slipstream characteristics, especially the downstream evolution of the wake, effectively by reducing the lateral movement of the mean streamwise vortex structures, despite the relatively small length scale of the rail cross-section. Perhaps surprisingly, the slipstream measured at the standard distance from the train centerplane, is found to be significantly reduced.

1. Introduction

High-speed trains have proven to be a viable intercity transportation method, due to their high transportation efficiency, both in terms of time and energy. Therefore, many countries, and especially those with high population densities, have built comprehensive high-speed rail networks, such as Germany, Japan, France and China. Historically, when high-speed train development began much of the research focus was on improvements in electric motor technology and reduction of frame weight, rather than improving train aerodynamics (Raghunathan et al., 2002). Indeed, rapid progress in the former two areas resulted in a remarkable speed-up of high-speed trains over the past few decades (Baker, 2010). As improvements in these areas are now likely to be more incremental, understanding the aerodynamic aspects is becoming increasingly important, such as train-induced flow - also known as slipstream. Slipstream is a safety hazard to commuters and trackside workers, and can even cause damage to infrastructure along track lines. Therefore, regulations are always enforced to restrict the maximum disturbance allowed caused by slipstream. This study employs the European regulations, which are promulgated by the European Committee for Standardisation (CEN) (Railway applications, 2013). CEN provides guidelines on how the

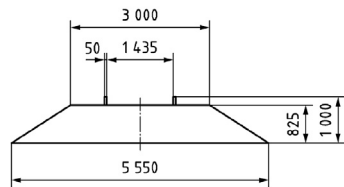
slipstream velocity should be measured and limitations of maximum allowable slipstream velocity, with which the train manufacturers have to comply. The Technical Specifications for Interoperability (TSI) (European union agency for railways, 2014) interprets the regulations specified in CEN, and provides specified annotations and requirements that HSTs have to meet to operate in the European Union.

By characterising the flow around a HST, Baker (2010) identified that typical HST slipstream is the combined effect of multiple flow features: the head pressure pulse, boundary layer development along the train body, the flow under the bogies and the wake behind the train. The development of slipstream has been proven to be highly dependent on the train geometry, for example the head/tail shape, length-to-height ratio and other attached features (Baker et al., 2001). Additionally, the entrainment of the surrounding air is greatly influenced by the operational environment, including the surrounding infrastructure, ground configuration and cross-wind. As an example, some research has been undertaken to evaluate HST aerodynamic performance with different ground configurations, such as: a viaduct or embankment (Cheli et al., 2010); flat ground or single-track ballast configuration (Bell et al., 2014); and ground roughness (Jönsson et al., 2014). However, according to the authors' knowledge, there is as yet no explicit study on the effect of rails

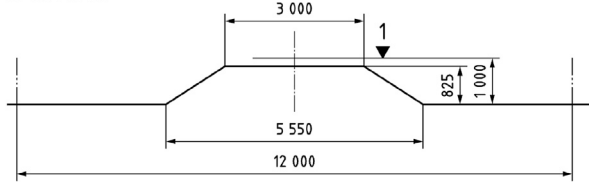
* Corresponding author.

E-mail address: shibo.wang@monash.edu (S. Wang).

CEN 2011



CEN 2013



Key

1 top of rail

Fig. 1. Illustration of the rule change on the inclusion of rails, based on the comparison of the ballast configurations specified in 2011 (Railway applications, 2011) and 2013 (Railway applications, 2013) CEN guidelines.

on HST slipstream characteristics, or even from the general aerodynamic viewpoint. Perhaps the most relevant previous research are the studies on train underbody flow and its loading on the track (Soper et al., 2017a, 2017b), which is also strongly correlated to the ballast flight phenomenon (Quinn et al., 2010). More recently, by using dynamic meshing, Paz et al. (Paz et al., 2017) modelled the sleepers in studying the HST underbody flow, and this improved the prediction for ballast flight. A potential reason for neglecting the impacts of rails might be that rails are a permanent feature of the ground configuration, and hence little in the way of direct modification can be done on this aspect to improve HST aerodynamic performance. Previous research e.g. (Bell et al., 2016a), and (Wang et al., 2018a), shows there is a pair of trailing vortices peeling off from the tail pillars and these are the dominant time-mean flow structure within the wake, and the downwash from the tail and self-induction pushes this vortical flow structure towards the ground towards the location of the rails. Due to this interaction, the rails will have some impact on the near-wake formation and downstream evolution, even though their length-scale (i.e., height) is minor compared to the scale of the train and wake flow structures.

As well as providing insight into the flow physics, this study also has practical significance. Firstly, reviewing actual methodologies for studying HST slipstream through computational analyses indicates that past numerical studies, either including or excluding rails, have been adopted. Despite this, there seems to be no study that investigates the differences introduced by including or not including rails. Thus, it can be unclear whether any observed differences in predictions are caused by differences in the train's geometry or the presence or absence of rails.

Secondly, no agreement has been achieved on the numerical prediction of HST slipstream in the CEN guidelines. In comparison, requirements and standards are specified for predicting the head pressure pulse, including the ballast configuration. Interestingly, the European standards on whether rails should be included for HST numerical simulations has changed in the last few years (Railway applications, 2009; Railway applications, 2011; Railway applications, 2013). Prior to 2011, CEN specified that the computational domain for studying train aerodynamics on an open track should include a ballast bed with rails extruding through the entire domain (Railway applications, 2009; Railway applications, 2011), as illustrated in Fig. 1 (a). In 2013 the standard changed, with the rails being removed from the ballast configurations (Railway applications, 2013) as presented in Fig. 1 (b); however, the reasons for this modification were not specified. While removal of the rails is not expected to significantly alter the head pressure pulse prediction, its impact on slipstream remains undetermined. Hopefully, the

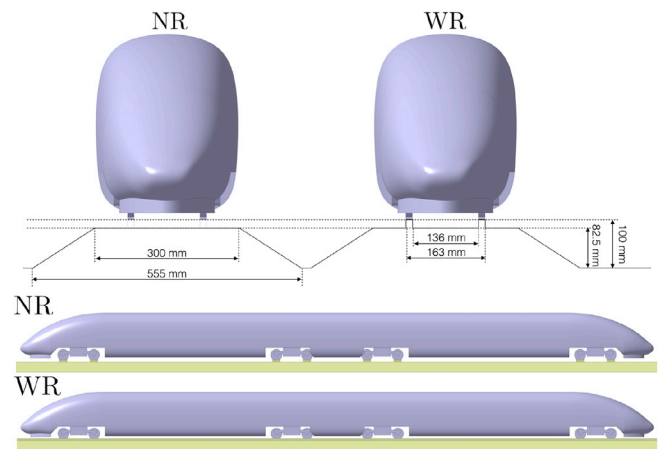


Fig. 2. The comparison between the ground configurations of NR and WR.

predictions from this study can provide some valuable information and insight in formulating the best practice for numerically predicting HST slipstream.

2. Numerical methodology

2.1. Geometry

The numerical train model used in this study is based on a 1/10th *Deutsche Bahn Inter-City-Express 3* (ICE3) high-speed train model, which is a widely operated train in European and Asian countries. ICE3 has a generic HST external geometry, and its Computer-Aided Design (CAD) model can be freely accessed from the DIN Standards Railway Committee (standards Committee R, 2014). This makes ICE3 an ideal HST model for train slipstream investigation. Compared with the aspect ratio (length-to-height) of a typical high-speed train, which is typically between 50 and 100:1, the length-width-height of the CAD model used for the simulations is significantly reduced to $5 \times 0.3 \times 0.4$ m corresponding to an aspect ratio of 12.5:1. This is a typical limitation for studying train aerodynamics both numerically and experimentally. The reduced train length will lead to a reduced boundary layer thickness towards the rear of the train. However, the formation of the time-mean trailing vortex pair seen in the numerical predictions is mainly driven by the geometry of the rear of the train, and hence it seems likely that a longer train will still maintain similar time-mean wake structures. Those structures should still be influenced by the channelling effect of the rails, although it is possible that the magnitude of the effect could be reduced. Additionally, to explicitly isolate the impacts of rails and reveal the corresponding underlying flow physics, the present study is based on an idealised HST model, as illustrated in Fig. 2. For example, some geometric details are omitted such as the inter-carriage gaps (Mizushima et al., 2007) and pantograph-catenary system (Pombo et al., 2009), while other key geometrical features that can significantly influence the slipstream are retained, for example the bogies and snowploughs. Even though this study aims to provide a better understanding of the impact of rails on a generic train model, the specific influences on different train models, especially on the realistic train geometries with a greater length-to-height ratio and more detailed features, may vary.

Two ground configurations, single track ballast with and without rails (referred as WR and NR (no rails), respectively), are modelled in this study. The dimensions of the WR ground configuration are based on the 2011 CEN specifications (Railway applications, 2011). The rail thickness is extended from 5 mm (CEN specified (Railway applications, 2011)) to 13.5 mm (wheel width) to reduce the complexity and quality of the mesh generation near the contact between the wheels and the rails. This approximation was made assuming that the rail width would not have a

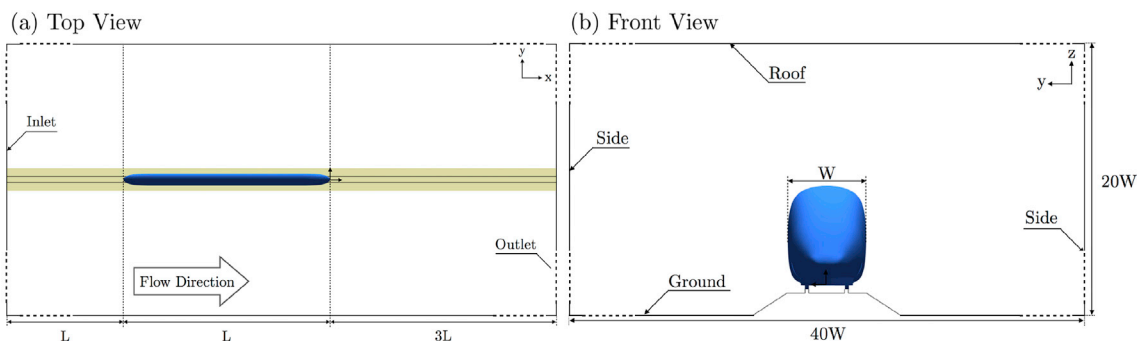


Fig. 3. Schematics of the computational domain: (a): top-view; (b): front-view (not to scale).

strong effect on the wake flow dynamics, while rail height might and, a posteriori, does appear to. According to the results, the rails interfere with the wake by acting as an obstacle to the transverse advection of the trailing vortical structures; therefore, the actual thickness is likely to be less critical than the height of the rails. As the result, the influence on the large-scale wake development caused by extending the rail thickness is expected to be limited. For the same reason, more geometrically accurate rails with an I-shape cross-section are expected to show a similar impact as rectangular-shaped rails do, as long as they primarily act as an obstacle to the transverse flow. The only difference between the WR and NR ground configuration is the existence of rails, all other dimensions remain identical, for example, the dimensions of the ballast and ground clearance.

For both NR and WR configurations, sleepers and ground roughness, which may affect the wake, are not explicitly modelled in the current study for the following reasons. Primarily, this because the sleeper configuration can vary on different tracks. For conventional ballast, with the sleepers located on crushed stones, the surface roughness is considerable. For more recent ballast systems, especially for high-speed trains, sleeperless track systems with sleepers positioned within the concrete track are becoming more widely adopted. Thus, it seems appropriate to undertake an initial study without the complexities of either sleepers or gravel roughness. Additionally, as a key objective of this paper is to examine the differences between numerically modelling train slipstreams, including and excluding rails, as both types of model have been adopted. Finally, the same inconsistency has been noted in the different versions of the related guidelines. In different scenarios, the sleepers are always omitted, while the inclusion of rails varies case by case. In the NR set up, the gap between the wheels and ballast is filled by extruding the (small) rectangular-shape wheel contact patch to the ballast surface. Interestingly, as indicated, compared with the original CEN specifications (Railway applications, 2011), the latest 2013 regulation (Railway applications, 2013) removes the requirement of modelling the rails on the ballast (equivalent to NR), but the reason for this modification was not specified.

2.2. Computational domain and boundary conditions

The layout of the computational domain is identical for both cases, for which the train model is positioned on a single ballast track in a computational domain consisting of hexahedral elements, and the ballast is extended through the entire computational domain. Therefore, the schematic of computational domain for the WR case is used as an example here to illustrate the general numerical set-up, as presented in Fig. 3.

Generally in this study, spatial dimensions are normalised by the train width (W) in the spanwise direction (y -direction), or by the length (L) of the train in the streamwise direction (x -direction), this will be made clear at the time. The origin of the coordinate system is positioned in the centre of track, at the height of the top of rails (TOR), with $x = 0$ corresponding to the tail tip. For consistency, the coordinate system remains identical,

regardless of the presence of the rails. As part of this study, the influence of the outflow length of the domain on slipstream predictions was investigated by undertaking limited simulations using an extended outflow length (changing from $37.5H$ to $100H$). These indicated that the near-wake predictions ($x/H < 20$) were effectively unchanged by using a longer outflow length.

The boundary conditions applied to the NR and WR cases are identical. At the inlet a uniform velocity boundary condition with a turbulence intensity of 1% is applied. The Reynolds number (based on W) of the incoming flow is 7.2×10^5 . These values are chosen for consistency to allow a validation with wind-tunnel experiments in a previous study (Wang et al., 2017). However, please note that they are not directly comparable to a full-scale operational environment. At the outlet boundary zero static pressure is specified, as is common in incompressible flow simulations. All train surfaces employ a no-slip wall boundary condition. Symmetry boundary conditions are applied at the top and

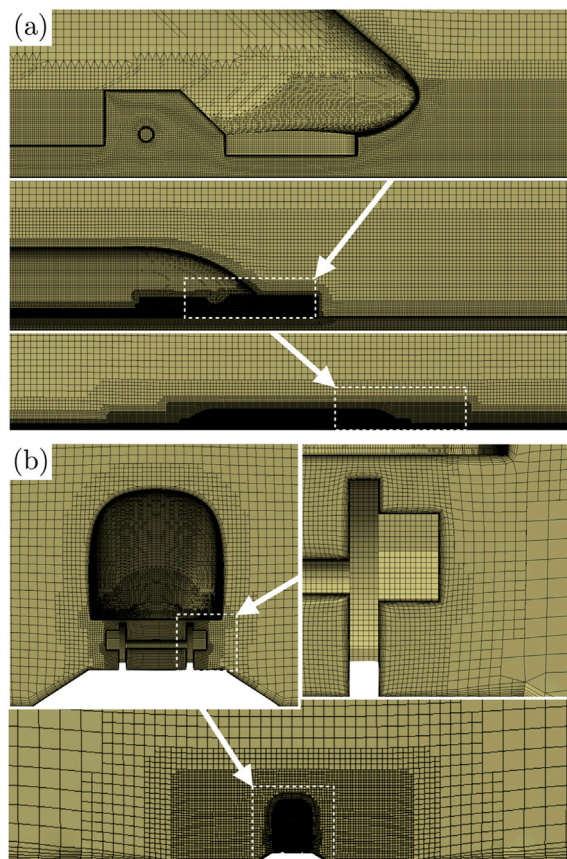


Fig. 4. The visualisation of grid refinement around the train based on WR: (a): centre-plane; (b): cross-section.

Table 1
Key meshing parameters.

	Train surface mesh	$0.00625H \sim 0.025H$
Cell size	Rails/contact patches surface mesh	$0.00625H \sim 0.025H$
	Under-body refinements	$0.00625H \sim 0.0125H$
	Wake refinements	$0.0125H \sim 0.05H$
	Far-field refinements	$0.1H \sim 0.4H$
	No. of inflation layers	10
	Train surface wall y^+	$1 \sim 20$

sides of the computational domain. To simulate the realistic condition of a moving train travelling through still air, where no relative motion exists between the air and the ground, a no-slip moving-wall condition at the freestream velocity (U_∞) is applied to the ground, including the ballast and rails (or the wheel contact patches for the NR configuration). The axes of the rotating wheel-sets are along the centrelines of the axles, and the wheels rotate at a constant angular velocity, with the speed at the rim equal to the speed of the moving ground. For the sake of achieving a clearer visualisation of the computational domain configuration, Fig. 3 is not drawn to scale.

2.3. Meshing strategy

These simulations apply a consistent meshing strategy between cases; therefore, the WR mesh is used as an example to demonstrate the meshing strategy. The overall meshing strategy is the Cartesian cut-cell approach, which allows mesh refinements around the train and in the wake, and a smooth transition between the higher- and lower-resolution regions is established. This is a common meshing strategy for numerical simulations (Muld et al., 2012; Hemida et al., 2014). In this study, the mesh concentration is accomplished by applying virtual refinement zones at target regions. For example, multiple levels of refinement zones are applied around the train and within the wake to effectively improve the accuracy at the critical regions, as illustrated in Fig. 4. The dimensions of refinement zones were finalised according to preliminary simulations to ensure that all important flow features are captured. A sudden change of the grid size between adjacent cells is avoided at all interfaces, including between the *inflation layer* and the hexahedral grid, and between two refinement zones, as illustrated in Fig. 4.

This method achieves a high uniform resolution within the slipstream measurement regions by accurately capturing the boundary layer development and induced flow separation generated by smaller-scale geometrical features. To capture the boundary-layer development, *inflation layers* are applied to all wall boundaries. All wall surfaces, including the train and ground, are covered by 10 inflation layers, with the thickness expanding at a ratio of 1.3 between adjacent layers. At train surfaces, y^+ lies in the range: $1 \sim 20$.

A mesh independence study was undertaken in a previous related study (Wang et al., 2017), which examined the ability of different turbulence models to capture different aspects of slipstream. The mesh independence study systematically examined the influence of surface cell size and the number of inflation layers, which resulted in the train surface wall y^+ varying from below 30 in the fine mesh to as high as 150 in the coarse mesh. In that study, the comparison between the performance of three sequentially refined grids (coarse, medium and fine) shows that the drag and slipstream predictions varied by less than 1 and 2% between the fine and medium grids. This study adopts the equivalent mesh settings of the fine grid, for which key meshing parameters are listed in Table 1. Based on these settings, the number of cells for the NR and WR cases are ~ 23 and 27 million, respectively. It can be seen that modelling the rails is computationally expensive, as in this study it is solely responsible for increasing the number of cells by 17.4%.

2.4. Solver description

The commercial CFD code *FLUENT*, a part of the ANSYS 16.2 software suite, is utilised to numerically model the flow field. To predict the highly turbulent HST slipstream, the pressure-based transient solver is employed. *Detached Eddy Simulation* (DES) is used to resolve large turbulence scales, and specifically, a variant known as *Improved-Delayed DES* (IDDES) is utilised. DES is a hybrid turbulence model that blends Reynolds-Averaged Navier-Stokes (RANS) modelling near boundaries with Large Eddy Simulation (LES) for the outer flow. This study employs a variation of DES model which known as IDDES. This model applies an *improved delayed shielding function* to achieve a higher accuracy for the RAN-LES blending region and improve the wall-modelling capability. Similar to the classic DES blending technique, IDDES also utilises RANS to resolve the boundary layer and applies LES to capture the transient flow features away from boundaries. The *Shear-Stress Transport* (SST) $k - \omega$ model is used for the RANS component within the overall IDDES model, due to its superior performance in modelling the near-wall boundary-layer regions with undefined separation points. IDDES has been extensively adopted to study the train aerodynamics, for example, in a study of slipstream assessment (Huang et al., 2016), and for underbody flows (Zhang et al., 2016). A fuller description of the theory behind the IDDES model is given in (Spalart, 2009). To start the time-dependent simulation, the flow field is initialised with a second-order accurate steady-state RANS simulation predicted with the SST-RANS model. The flow is then subsequently simulated with the IDDES turbulence model.

The solver timestep was $\Delta t = 0.0025T_{ref}$, where T_{ref} is a reference time scale based on the train height and freestream velocity, given by $T_{ref} = H/U_\infty$. This timestep was chosen to maintain the Courant number of the typical smallest cells to be less than unity, which is suggested for DES-type simulations. Hence, the non-iterative Fractional-Step Scheme can be used to integrate forward in time. The recommended bounded second-order implicit formulation is applied for transient equations. For the spatial discretisation, except for the momentum equation for which bounded central differencing is utilised, the convective terms in other transport equations are discretised with the second-order upwind scheme. Unsteady statistics results are collected after the flow field has reached an asymptotic statistical state, which is checked by comparing the statistics with predictions from shorter sampling intervals. Unsteady statistics are sampled over $195 T_{ref}$, which approximately equals to the time taken for the fluid to advect through the entire domain 3 times, or to pass the length of the train approximately 15 times. The computational time for each simulation is approximately 40 KCPU hours on the Australia National Computing Infrastructure (NCI) high-performance computing cluster, with typical runs using $128 \sim 256$ cores.

2.5. Validation

Validation of the numerical model was presented in a previous study (Wang et al., 2017), which evaluated the effects of the key numerical settings on predicting the slipstream, including the selected turbulence model, the grid resolution and the time-step, and provided guidelines for selection of those settings for subsequent studies. The current research utilises the best choice numerical settings derived from that study (Wang et al., 2017). The validation was carried out by comparing the results of time-averaged and dynamic flow features between numerical simulation predictions and wind-tunnel measurements (Bell et al., 2016a, 2016b). The train model in this current study is identical to the one used in the validation study, and the flow conditions of the two studies are very similar. However, the ground boundary condition varies: the previous study utilised a stationary-ground configuration to replicate the wind-tunnel experimental environment, while this study adopts a moving-ground configuration to match the actual relative velocity between the ground and the train in real applications. The feasibility of the present numerical approach to resolve the slipstream flow under

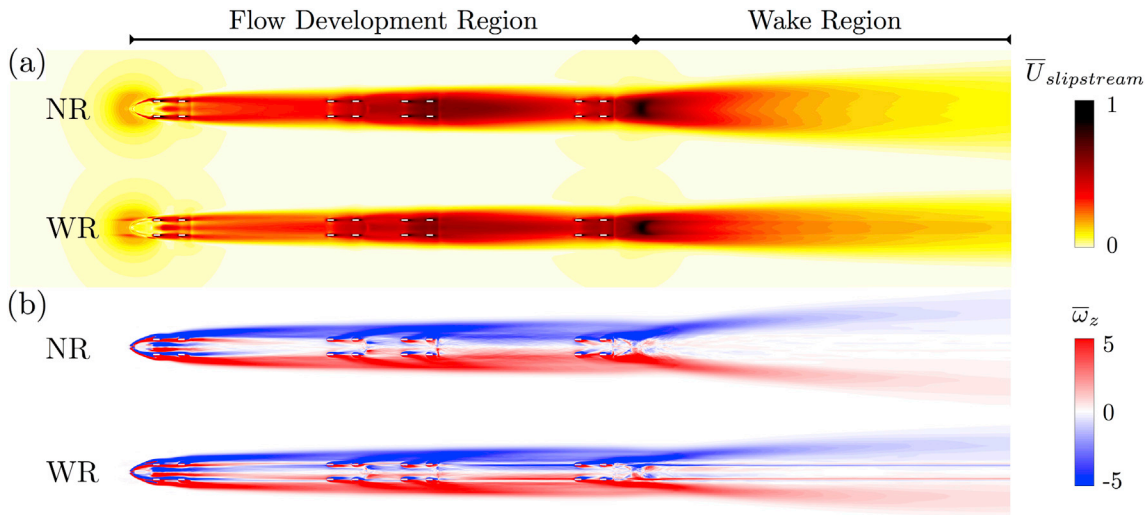


Fig. 5. The overall comparison of rail effects within the flow development and wake regions visualised by (a): $\bar{U}_{slipstream}$ and (b): \bar{w}_z at a horizontal plane in the middle of the underbody and TOR.

different ground conditions has been verified by the authors in another study (Wang et al., 2018b), and the potential flow alteration that can be introduced by the stationary ground boundary layer was also investigated. According to that study (Wang et al., 2018b), the moving-ground condition chosen for this study is expected to eliminate the ground boundary layer development, which has an influence on the wake, as identified in the previous study. An underlying assumption is that the numerical mesh and settings that are capable of capturing the growth of the ground boundary layer and its interaction with the train-induced wake structures, are also appropriate for the simpler case in which the stationary ground boundary layer is not present. For reference purposes, the statistical slipstream profiles of the experimental measurements and numerical simulations adapted from the validation study (Wang et al., 2017) have been included in Fig. 14. The two validation cases in Fig. 14 show in general good agreement, even though some deviation is apparent between the numerical and experimental results, especially the peak values within the wake region. The difference in background turbulence levels between the simulations and experiments may be one possible cause, and the peak slipstream velocity is recorded about 8H behind the tail, which is moving beyond the optimal working section of the tunnel. A more detailed discussion on the two validation cases is presented in (Wang et al., 2017). The physical experiment was implemented in the

Monash University 1.4 MW closed-circuit wind tunnel, and a detailed description regarding the experimental set-up and results can be found in (Bell et al., 2017).

3. Results and analysis

The strength of slipstream is quantified by the *slipstream velocity* ($U_{slipstream}$). Slipstream, i.e., train-induced wind, velocity is naturally defined based on a ground-fixed (GF) stationary reference frame, while CFD simulations are based on the train-fixed (TF) reference frame. Therefore, a change of frame is required, as expressed through the equations below:

$$U_{slipstream} = \sqrt{(U_{GF}^2 + V_{GF}^2)}, \tag{1}$$

where

$$U_{GF} = \frac{U_\infty - U_{TF}}{U_\infty}, V_{GF} = \frac{V_{TF}}{U_\infty}. \tag{2}$$

The subscripts *GF* and *TF* in equations (1) and (2) indicate *ground-fixed* and *train-fixed* reference frames, respectively. Velocities, including

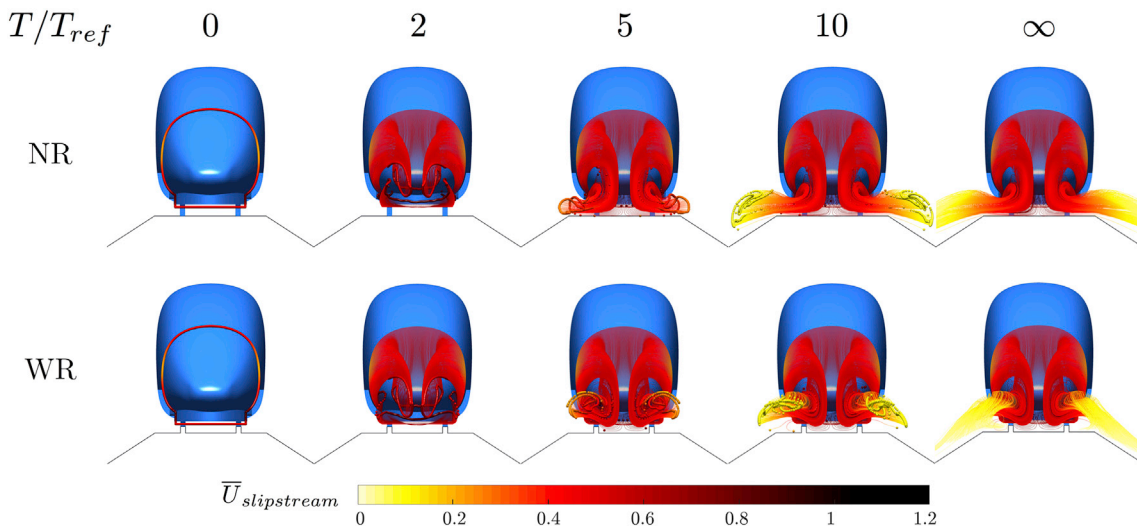


Fig. 6. The interaction between the rails and the tracer particles released from near the tail as time elapses.

slipstream velocities, are typically normalised by the freestream velocity (U_∞). Also note that slipstream only takes account of the downstream (U) and transverse (V) components of the velocity, but not the vertical velocity component.

Initially, the effects of rails on the slipstream characteristics are studied by comparing the time-averaged flow structures between the NR and WR configurations in Section 3.1, allowing the mechanism of how the rails interfere with the slipstream development to be revealed. The effects on the transient wake features are then studied in Section 3.2. Following this, how the altered time-averaged and transient flow structures further affects slipstream assessment is investigated, based on statistical slipstream profiles and gust analysis in Section 3.3.

3.1. Time-averaged flow structure

To understand the effects of rails on each stage of the slipstream development, the entire flow field is divided into a flow development region and a wake region, as shown in Fig. 5, and the effects on each region are investigated.

The flow development region extends approximately from the head to the tail of the train, and the wake region starts from the tail and extends downstream to where slipstream becomes negligible. Fig. 5 shows that the effects of rails within the flow development region are limited to the region in close proximity to the rails. In comparison, a significant difference is observed within the wake region, and both time-averaged slipstream velocity ($\bar{U}_{\text{slipstream}}$) and z -vorticity ($\bar{\omega}_z$) contours demonstrate that the presence of rails narrows the wake.

According to the previous studies (Bell et al., 2016a; Wang et al., 2017), the dominant mean wake structure behind a HST is characterised by a pair of longitudinal counter-rotating vortices. The impact of rails on the formation of this coherent flow structure is visualised by the motion of tracer particles, as shown in Fig. 6. The particles are released at $x = -0.5H$, and 75 mm (in full-scale) offset from the train surface. The wake development is visualised by tracking the movement of these particles in a time-mean flow field, with the tracers coloured by $\bar{U}_{\text{slipstream}}$.

Fig. 6 shows identical patterns for the two models before the flow structures impinge on the ground. The trailing vortex pair is generated as the boundary layer separates from the curved edge between the top and side surface of the tail. The variation in the wake is initiated when the downwash from the tail approaches the ballast. Without the rails, the wake can freely move outwards in the transverse direction (due to the presence of image vortices within the ballast). In comparison, the presence of the rails obstructs the transverse movement of the streamwise vortices; thus, the wake structures appear to shift upwards and roll over the rails. The rails possess a lock-in effect on the trailing vortices, by attempting to keep the trailing vortex pair between the rails. This bulk effect is probably due to a combination of a number of different effects including: generation of opposite-sign streamwise vorticity at the rail boundaries, which may weaken the streamwise vortices through diffusion and cross-annihilation; preventing the natural self-propulsion of the vortex pair to approach the ground because of geometrical blockage; and forcing the vortex pair to move upwards to pass over the rails, thereby weakening the induced sideways motion caused by the image vortices and thus reducing sideways movement. The lock-in effect of the rails can be clearly demonstrated through the time-mean transverse wall-shear stress ($\vec{\tau}_y$) on the ballast, as plotted in Fig. 7. Without the rails, the relative motion between the wake and ballast in the spanwise direction causes a widespread high $\vec{\tau}_y$ magnitude region at the top surface of the ballast. In contrast, the presence of rails locks this wake structure between the rails, showing a concentrated $\vec{\tau}_y$ alteration. It is also clear that the rails cause the shear stress to change sign further out. This is indicative of reversed flow generated by the outward separated flow over the rails. Again, this is likely to further weaken the vortex pair, leading to reduced sideways motion. An alternative view is to note that to mostly lock the swirling wake structures between the rails, a strong side

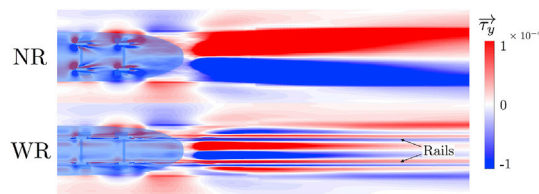


Fig. 7. The lock-in effect visualised by the time-mean transverse wall-shear stress at the ballast surface.

aerodynamic loading is exerted on the rails, which is quantitatively illustrated by the C_p profiles at the ballast cross-section at $x = 0.5H$, as shown in Fig. 8. Fig. 8 illustrates that a strong positive pressure exerted on the inner surfaces of the rails, attempting to push the rails outwards. In comparison, a small pressure exerted on the outer sides of the rails that pushes the rails inwards is caused due to the corner recirculation region formed during the rolling-over of the trailing vortices as they advect outwards. Additionally, a significant pressure drop is determined between the inner and outer sides of the rails. The high pressure region between the rails is associated with the impingement of the downwash, and the lock-in effect causes a pressure drop across the rails. Despite these significant effects, the difference in aerodynamic loading on the ballast slopes between the NR and WR cases is negligible.

The sideways propagation of the trailing vortices is quantitatively depicted by time-averaged x -vorticity ($\bar{\omega}_x$), in-surface projected velocity vectors with superimposed vortex cross-sectional boundaries on six consecutive vertical planes between $x = 0.5H$ and $5H$, as presented in Fig. 9.

Only the left half of the flow field is presented in Fig. 9 due to the bilateral symmetry of mean flow structure. The boundary of the trailing vortex structure is defined by the iso-line of $\Gamma_2 = 2/\pi$, which is a common vortex identification method, refer to (Graftieaux et al., 2001) for a full description. Additionally, the core of a vortex is indicated by a green asterisk, which is determined by the maximum local value of the Γ_1 coefficient (again see (Graftieaux et al., 2001)). The crosses (+) and circles (o) in Fig. 9 represent the trackside ($z = 0.05H$) and platform ($z = 0.35H$) slipstream measurement locations, respectively, based on the TSI specifications (European union agency for railways, 2014). Fig. 9 illustrates that the wake structure in proximity to the tail is effectively identical in the two cases, but a difference accumulates when the streamwise vortex pair propagates further downstream. Consistent with the results shown by the particle tracers in Fig. 6, the rails effectively obstruct the wake's spanwise motion, and the trailing vortices have to roll over the rails and then propagate further downstream. The positive $\bar{\omega}_x$ regions generated at the corner of the rails are indications of the rails' obstruction, which is more obvious during the roll-over process within the near wake. This secondary vortex is highlighted through a close-up view of the flow around the rails at $x = 1H$, as depicted in Fig. 10. Fig. 10 clearly shows that the rails act as an obstacle or fence to the near-ground flow which moves outwards, and as a result the flow separates at the edge and forms a secondary vortex. Please note that the typical effective Reynolds number, based on the in-surface projected velocity and rail height, in the neighbourhood of the rails is in the order of 10^4 . This is significantly lower than the value in a full-scale operational environment. However, based on a previous study of the flow over a solid

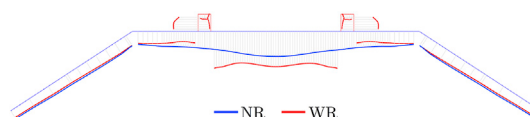


Fig. 8. The comparison of C_p profiles at the ballast surface at $x = 0.5H$.

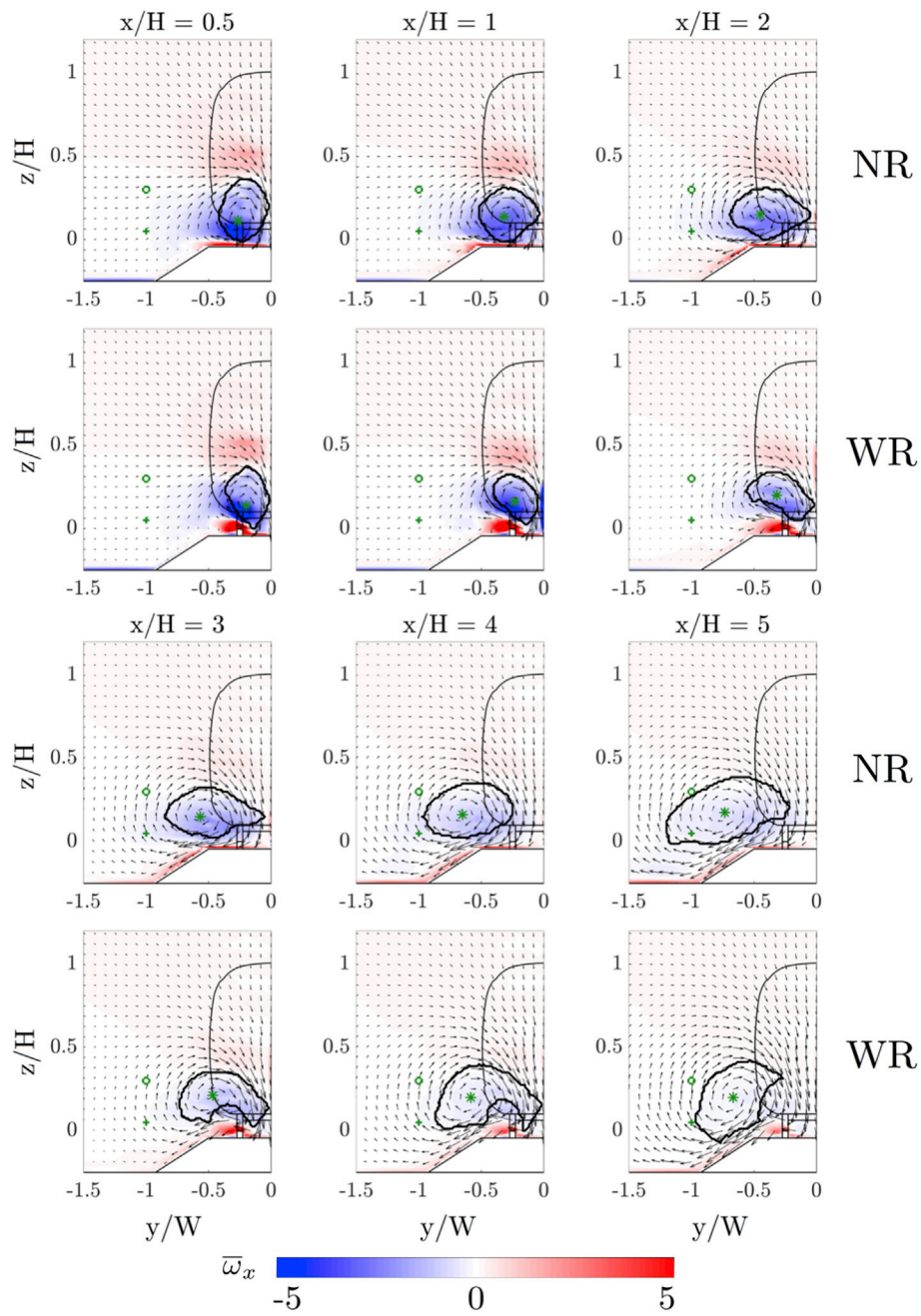


Fig. 9. The wake propagation visualised by \bar{w}_x contour and in-surface projected velocity vectors at 6 consecutive vertical planes from $x = 0.5 \sim 5H$ (+: trackside slipstream measurement location; o: platform slipstream measurement location; *: vortex core).

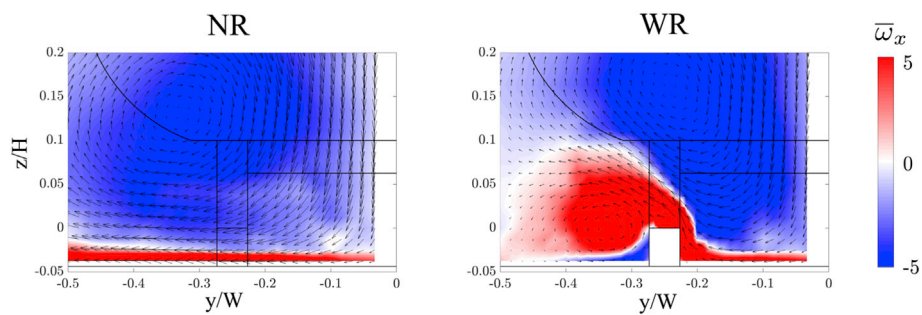


Fig. 10. A close-up view of the flow around the rails visualised by \bar{w}_x contour at $x = 1H$ and in-surface projected velocity vectors.

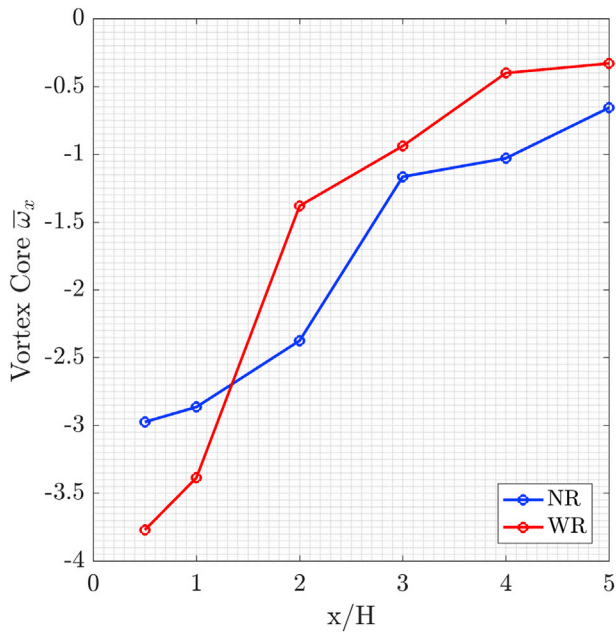


Fig. 11. The change of $\bar{\omega}_x$ at the vortex cores in the longitudinal downstream direction.

fence (Fang et al., 1997), the mean flow field is qualitatively consistent across the Reynolds number range between $4 \times 10^3 \sim 1 \times 10^7$. Additionally, Castro et al. (Castro and Robins, 1977) showed that for the flow around a surface-mounted cube, the flow separation is fixed at the leading edge, and the shear layer appeared to be turbulent and showed Reynolds number independence beyond a value of 3×10^3 . Therefore, even though the crossing flow around the scaled model is significantly lower than for the full-scale case, a similar flow structure is expected to be seen at higher Reynolds numbers. Additionally, the rails deform the shape of the trailing vortices during roll-over, as illustrated in Fig. 9.

Furthermore, the decay in the strength of the trailing vortices is quantified by the change of the peak vortex-core streamwise vorticity ($\bar{\omega}_x$) in the longitudinal direction, as presented in Fig. 11.

From $x = 0.5H$ to $5H$, the vorticity magnitude drops from 2.97 to 0.66 at an average rate of 0.51, and 3.77 to 0.33 at an average rate of 0.76, for the NR and WR configurations, respectively. Overcoming the obstruction of the rails causes a rapid loss of vortex strength, and results in a greater downstream decay rate of $\bar{\omega}_x$. This is presumably due to the secondary vorticity generated at the rail surfaces that separates and then diffuses and cross-annihilates with the primary vorticity of the time-mean vortex pair. For example, the fastest decay occurs between $x/H = 0.5$ and 2, where the vortex cores are approximately positioned directly above the rails during the roll-over process. Except for the high decay region of $x/H = 0.5 \sim 2$ for WR due to the interference of rails, the overall decay rate further downstream is quantitatively similar between the NR and WR configurations.

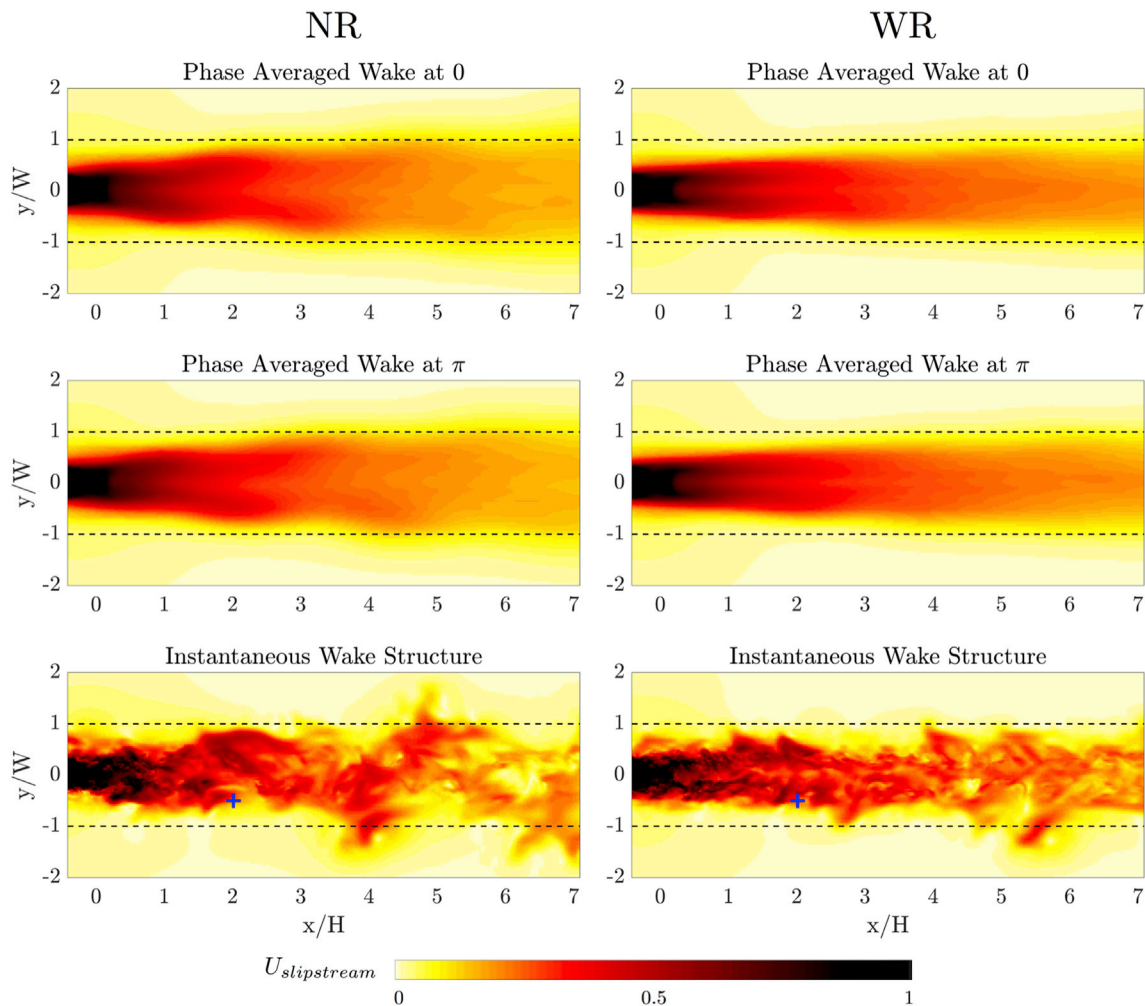


Fig. 12. The wake dynamics visualised by the phase-averaged and instantaneous $U_{slipstream}$ at the $z = 0.05H$ (+: phase-averaging reference point).

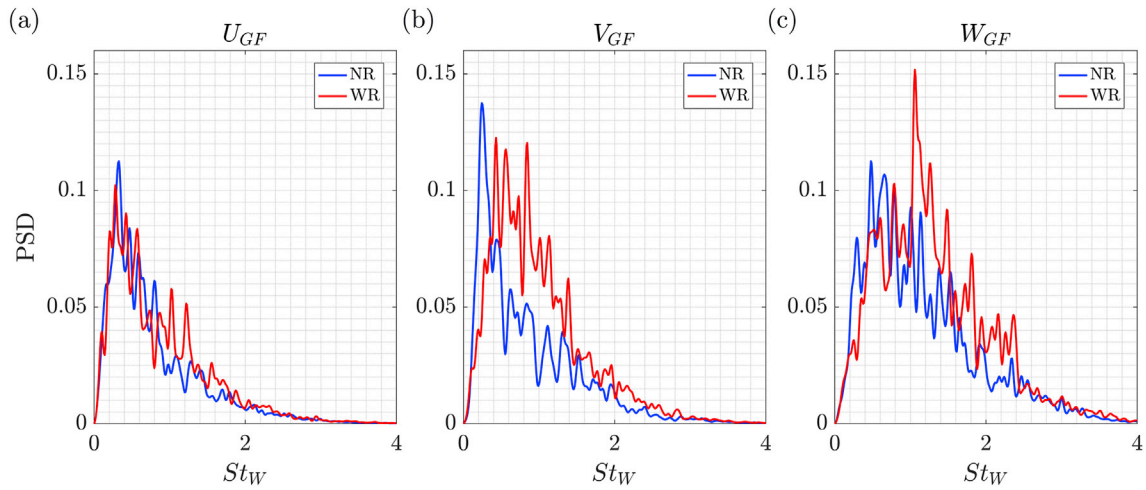


Fig. 13. The power density spectral content of the three velocity components at the phase-averaging reference point ($[2H, -0.5W, 0.05H]$).

3.2. Wake dynamics

In this study, the effects of rails on the wake dynamics are illustrated by phase-averaging $U_{slipstream}$ on a horizontal plane at $z = 0.05H$, as presented in Fig. 12. The V_{GF} measured at the point with coordinates ($[2H, -0.5W, 0.05H]$) is utilised as the reference signal for this phase averaging, the location of the reference point is visualised by the blue crosses in Fig. 12. The two black dashed lines represent the locations important for slipstream assessments according to the TSI specifications (European union agency for railways, 2014). The first and second rows in Fig. 12 illustrate the wake profile that is half a period apart, and the third column presents the instantaneous wake structure at an arbitrary time instance. Fig. 12 shows that without the presence of rails, the wake structure oscillates with a greater amplitude in the spanwise direction. On the other hand, both the NR and WR models determine an identical longitudinal wavelength of approximately $2H$, showing no significant dependence between the spanwise oscillating frequency and the presence or absence of rails.

The frequency response of the dynamic wake structure is studied using power spectrum analysis of the velocity components at the phase-averaging reference points (indicated as blue crosses in Fig. 12), and the results are presented in Fig. 13.

The frequency in this study is non-dimensionalised through the Strouhal number ($St_W = fW/U_\infty$), which is calculated based on the train width (W) and upstream (or train) velocity (U_∞). The power spectral density (PSD) for $St_W = 0 \sim 4$ is presented in Fig. 13 for each velocity component. Fig. 13 (a) shows that both models have an identical peak frequency of around 0.3 in U_{GF} , which implies that the effect of rails on the longitudinal pulsing is limited, as would be expected. In comparison, NR model indicates a clear peak frequency of 0.21 in the V_{GF} signal, while the WR model shows a broader spectrum peaking at a higher frequency, as shown in Fig. 13 (b). This implies that a more identifiable spanwise oscillation is established without the presence of the rails, while smaller-scale turbulent features are introduced by the transverse interaction between the rails and wake. According to Fig. 13 (c), an identifiable peak frequency of $St = 1.05$ is determined for the WR model from the W_{GF} signal, while this peak is not captured for the NR model. A possible explanation is that this peak frequency is due to an oscillation associated with the vertical motion of the trailing vortices introduced by rails during the roll-over process, as illustrated in Fig. 9. Of course, the frequency content is likely to be position dependent, as indicated by the visualisations of the instantaneous flow in Fig. 12. However, clearly the rails have a strong effect on the downstream wake evolution, including its spectral content.

Table 2

Critical values from the statistical slipstream profile analysis.

	NR		WR	
	Maximum	Location (x/H)	Maximum	Location (x/H)
Trackside height ($z = 0.05H$)				
$\bar{U}_{slipstream}$	0.110	5.50	0.078	-12.63
$\sigma_{slipstream}$	0.098	3.82	0.063	5.61
$U_{slipstream,max}$	0.300	4.66	0.194	6.61
Platform height ($z = 0.35H$)				
$\bar{U}_{slipstream}$	0.089	-12.57	0.088	-12.57
$\sigma_{slipstream}$	0.037	5.03	0.026	18.06
$U_{slipstream,max}$	0.119	8.50	0.089	-12.57

3.3. Slipstream assessment

In this study, the quantification of slipstream is studied from two perspectives: statistical slipstream profiles and gust analysis. The statistical slipstream profiles illustrate the time-average and standard derivation of the slipstream velocity at the TSI specified assessment locations, and thereby, provide an expected maximum slipstream velocity ($U_{slipstream,max}$) by adding twice the standard deviation to the mean slipstream velocity signal. As an alternative that tries to replicate the result from full-scale moving-train field measurements as laid out under the TSI specifications (European union agency for railways, 2014), gust analysis uses an ensemble of the temporal slipstream data to estimate the maximum slipstream induced. Details are provided below.

3.3.1. Statistical slipstream profiles

The statistical slipstream assessment is taken at both the TSI specified trackside height ($z = 0.05H$) and platform height ($z = 0.35H$), over the longitudinal displacement of $-15H \leq x \leq 30H$. The time-average and standard deviation of the slipstream velocity ($U_{slipstream}$), together with the individual streamwise (U_{GF}) and spanwise (V_{GF}) velocity components, at the two measurement heights, are plotted against streamwise position in Fig. 14, with the critical values listed in Table 2. The maximum expected slipstream velocity ($U_{slipstream,max}$), which is defined as $\bar{U}_{slipstream} + 2\sigma_{slipstream}$, predicts the upper limit of the slipstream velocity based on a 95% confidence interval, assuming normally distributed samples. The experimental measurements and associated numerical validation are added to Fig. 14 for validation and reference, and the comparison provides reasonable confidence in the numerical model. The main obvious variation between the numerical predictions (for the validation case) and wind-tunnel measurements occur in the

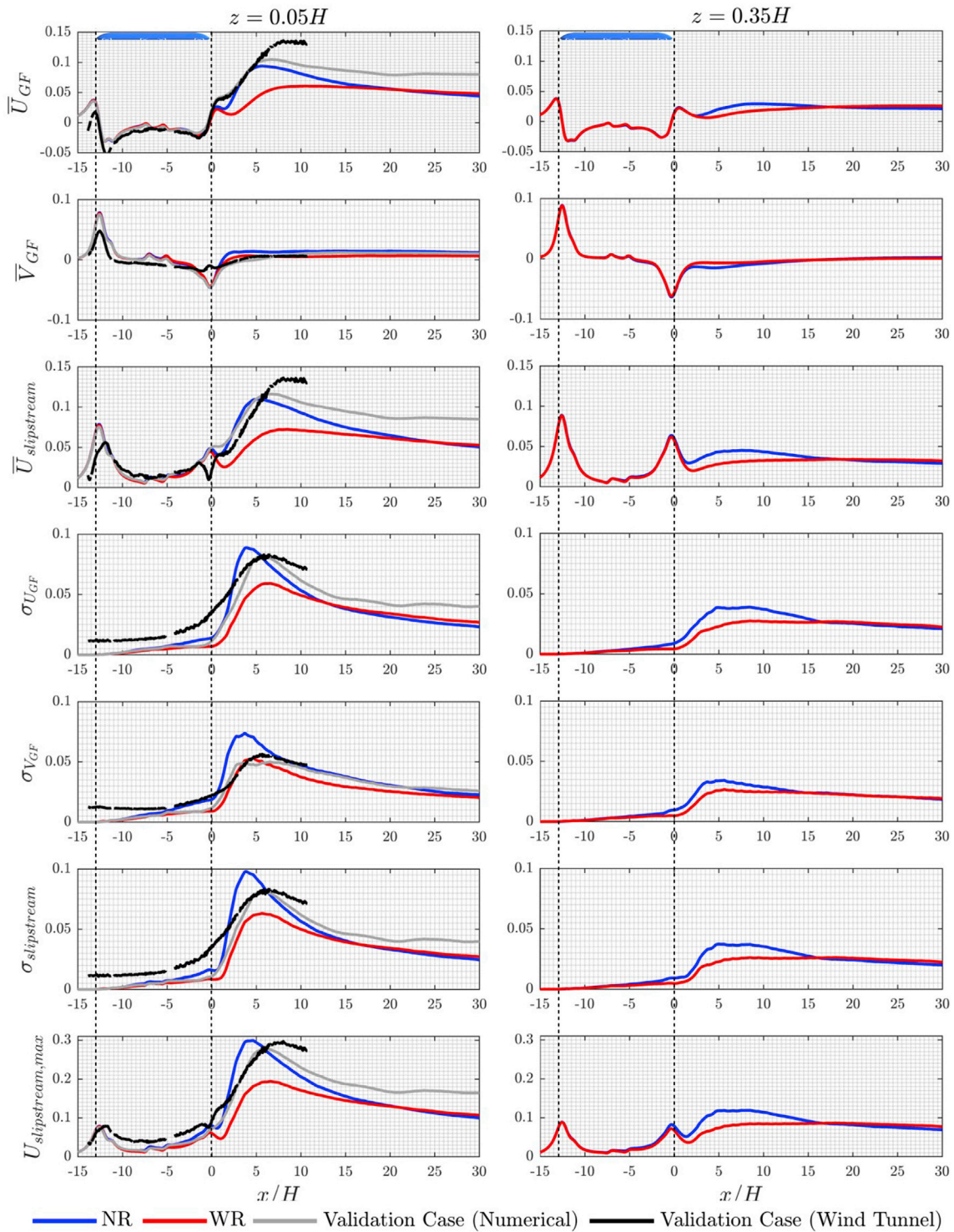


Fig. 14. The comparison of statistical slipstream profiles between NR and WR measured at the trackside ($z = 0.05H$) and platform ($z = 0.35H$) heights. The wind-tunnel measurements (Bell et al., 2017) and associated numerical simulations (Wang et al., 2017) at the $z = 0.05H$ are provided for reference. Note the validation cases adopt a different ground boundary condition as discussed in Section 2.5. Here σ represents standard deviation.

intermediate wake region, where the differences can be introduced from both the modelling and measurements. Numerically, slight simplification of the train model may alter the near/intermediate-wake results; while, the discrepancy in the intermediate wake ($x/H = 5 \sim 10H$) may be partially because these measurements were taken beyond the optimal working section of the tunnel. The deviations upstream of the tail are consistent with background wind-tunnel turbulence. A more detailed discussion regarding the match between the predictions and

measurements can be found in (Wang et al., 2017). In particular, note that the validation cases utilise a different ground boundary condition, and the slipstream profiles imply that the ground boundary layer can affect the magnitude and occurrence of the peak slipstream quantities. A detailed study of the effects of the ground boundary conditions is presented in (Wang et al., 2018b). The key finding of that study was to identify two ways that the ground boundary condition influences slipstream: (i) through directly altering the wake due to ground boundary

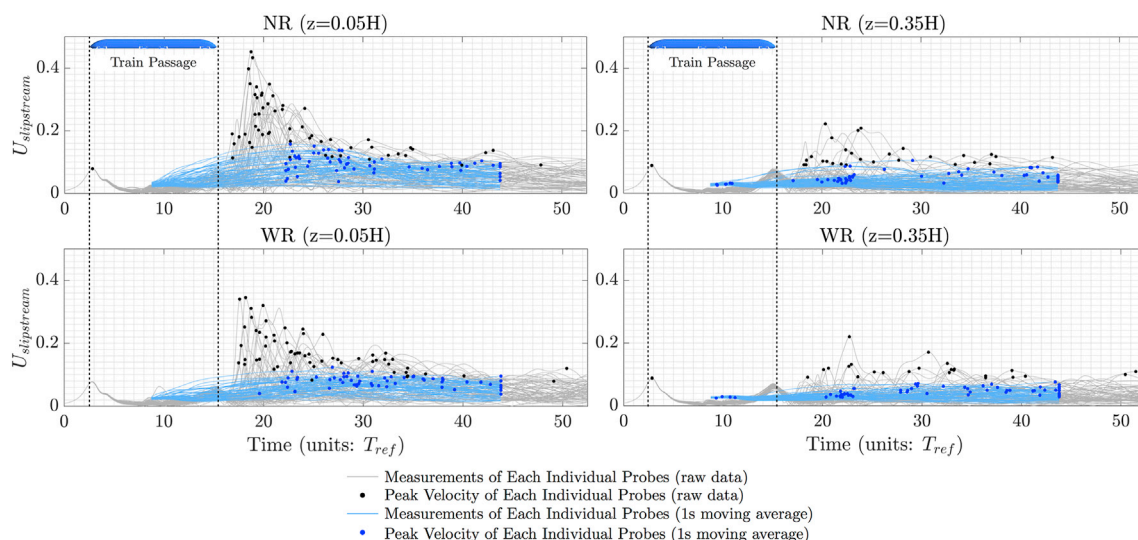


Fig. 15. The results of Gust Analysis based on the *Moving Probe Technique* under TSI specifications.

layer development, and (ii) through indirect widening of the wake by deformation of the trailing vortices.

As shown in Fig. 14, the NR and WR models share an identical $U_{slipstream,max}$ prior to the tail. Further downstream, although the rails alter the measurements at both heights, the alteration is more significant at a lower height. As illustrated previously in Fig. 9, the energy-containing vortex core shifts closer to the slipstream measurement location in the NR model causing a significant increase in \bar{U}_{GF} , and further altering $\bar{U}_{slipstream}$. In comparison, the impact on \bar{V}_{GF} is insignificant. By keeping the trailing vortices closer to the spanwise centre-plane in the WR model, both $\sigma_{U_{GF}}$ and $\sigma_{V_{GF}}$ within the wake at measurement locations are reduced. Due to the altered flow caused by the rails, especially in the near-wake region, the difference in $U_{slipstream,max}$ starts approximately from $x = 0H$ and ends at $x = 15H$. In general, the presence of rails alters the prediction of the $U_{slipstream,max}$ profile in causing (i) a significant decrease in the peak velocity, and (ii) a delay in its occurrence to further downstream.

3.3.2. Gust analysis

The TSI specification (European union agency for railways, 2014) outlines how the slipstream velocity should be measured under field testing and defines the procedure for calculating the maximum slipstream velocity (also known as the *TSI value*). Very briefly, the procedure proscribes using probes at fixed positions to record the slipstream velocity as the train passes. A 1-s running-averaging is applied to these time signals, with 20 independent recordings required. The TSI value corresponds to the peak slipstream value recorded. The TSI value is an important parameter that is compared with a maximum allowable slipstream velocity specified by TSI, in order for a train prototype to satisfy the regulations on slipstream. Numerically, *Gust Analysis*, originally proposed by Muld et al. (2014), tries to artificially replicate the field measurements, by using moving probes which pass through the computational domain parallel to the train. This approach is then equivalent to the ground-based experimental approach. The gust analysis in this study is performed with the *Moving Probe Technique* consistent with TSI regulations (European union agency for railways, 2014). A fuller description of the computational procedure associated with the *Moving Probe Technique* can be found in (Wang et al., 2017). As a result, the raw artificial probe measurements (ground-fixed frame) are shown by grey curves, where the peak measurements are highlighted with black dot points. After applying a 1-s running-average, as required by (European union agency for railways, 2014), the filtered data are plotted by blue curves, with the peak values highlighted by blue dot points. The results of probe

Table 3

Critical values from the gust analysis. The numbers in the brackets are the raw data without 1s moving average.

		$z = 0.05H$	$z = 0.35H$
NR	\bar{U}_{peak}	0.095 (0.204)	0.050 (0.105)
	$\sigma_{U_{peak}}$	0.027 (0.092)	0.018 (0.030)
	$U_{TSI,max}$	0.150 (0.389)	0.086 (0.166)
WR	\bar{U}_{peak}	0.079 (0.175)	0.045 (0.100)
	$\sigma_{U_{peak}}$	0.018 (0.065)	0.013 (0.023)
	$U_{TSI,max}$	0.114 (0.303)	0.072 (0.145)

measurements are illustrated in Fig. 15, and the corresponding critical values and calculations of the *TSI values* are listed in Table 3.

Compared to measurements at the platform height ($z = 0.35H$), the impact of rails is even more significant at the trackside height ($z = 0.05H$). According to the scattered distribution of the peak recorded velocities (plotted as black dots in Fig. 15) at the trackside height, the NR model shows a higher probability of recording a greater slipstream velocity immediately after the train passage. Both the NR and WR models demonstrate a right-skewed distribution, while a “sharper” peak is identified in the NR model. Ultimately, the absence of the rails can significantly increase the maximum predicted slipstream velocity ($U_{TSI,max}$) by 31.6% from 0.114 to 0.15. Therefore, the evaluation of the *TSI value* shows a strong dependence on the presence or absence of rails. Thus, it is interesting that the TSI guidelines have dropped the requirement to include rails from the 2013 regulations, although noting that this is a conservative approach since the inclusion of rails appears to lower the maximum slipstream prediction.

4. Conclusion

In conclusion, the effect of rails on slipstream characteristics is investigated by studying the alteration to the wake flow structures and the impact on the slipstream assessment. Compared with the minimal change to the near-train flow as the air flows past the train, the rails mainly alter the HST wake structures, especially within the near-wake region when the downwash from the tail impinges on the ballast. The rails alter the downstream wake evolution by obstructing the transverse movement of streamwise wake structures, and this affects both time-averaged and transient wake features. Without the rails, the time-mean trailing vortices move further away from each other in the cross-stream direction as they propagate downstream. The presence of rails obstruct

this transverse motion, as the trailing vortices have to roll over the rails during propagation. The interaction between the wake and rails causes a strong sideways loading on the rails and is associated with a greater decay rate of the vortex strength, probably due to diffusion and cross-annihilation with secondary vorticity generated at the rail surfaces. Additionally, the rails reduce the amplitude and coherence of the spanwise oscillation of the wake structure, while the change to the longitudinal wavelength is negligible. The above changes to time-averaged and transient flow features significantly modify slipstream development. Both statistical and gust analyses determine that the peak slipstream velocity in the wake is reduced and its downstream location is delayed by the presence of rails. Furthermore, this study indicates that the maximum predicted slipstream velocity (*TSI value*) has a strong dependence on the presence or absence of rails, reducing its value by $\sim 30\%$. Note that this study is focused on specifically isolating the effects of rails. Thus, some simplifications to the train geometry and ballast are implemented for this idealised model. In particular, detailed features such as the presence of sleepers and ballast roughness, which are likely to have a non-negligible effect on the wake, are not included in this study. Also note that the bogies are also simplified and the gaps between carriages omitted. Although those additional details are likely to have an influence on wake development, this study suggests that the impact of rails will still be significant.

References

- Baker, C., 2010. The flow around high speed trains. *J. Wind Eng. Ind. Aerod.* 98 (6), 277–298.
- Baker, C.J., Dalley, S.J., Johnson, T., Quinn, A., Wright, N.G., 2001. The slipstream and wake of a high-speed train. *Proc. Inst. Mech. Eng. - Part F J. Rail Rapid Transit* 215 (2), 83–99.
- Bell, J.R., Burton, D., Thompson, M.C., Herbst, A., Sheridan, J., 2014. Wind tunnel analysis of the slipstream and wake of a high-speed train. *J. Wind Eng. Ind. Aerod.* 134, 122–138.
- Bell, J.R., Burton, D., Thompson, M.C., Herbst, A.H., Sheridan, J., 2016a. Flow topology and unsteady features of the wake of a generic high-speed train. *J. Fluid Struct.* 61, 168–183.
- Bell, J.R., Burton, D., Thompson, M.C., Herbst, A.H., Sheridan, J., 2016b. Dynamics of trailing vortices in the wake of a generic high-speed train. *J. Fluid Struct.* 65, 238–256.
- Bell, J.R., Burton, D., Thompson, M.C., Herbst, A.H., Sheridan, J., 2017. A wind-tunnel methodology for assessing the slipstream of high-speed trains. *J. Wind Eng. Ind. Aerod.* 166, 1–19.
- Castro, I., Robins, A., 1977. The flow around a surface-mounted cube in uniform and turbulent streams. *J. Fluid Mech.* 79 (2), 307–335.
- Cheli, F., Corradi, R., Rocchi, D., Tomasini, G., Maestrini, E., 2010. Wind tunnel tests on train scale models to investigate the effect of infrastructure scenario. *J. Wind Eng. Ind. Aerod.* 98 (6), 353–362.
- European union agency for railways, 2014. Commission Regulation (EU) No 1302/2014 concerning a technical specification for interoperability relating to the ‘rolling stock — locomotives and passenger rolling stock’ subsystem of the rail system. *Off. J. Eur. Union*.
- Fang, F.-M., Hsieh, W., Jong, S., She, J., 1997. Unsteady turbulent flow past solid fence. *J. Hydraul. Eng.* 123 (6), 560–565.
- Graftieaux, L., Michard, M., Grosjean, N., 2001. Combining PIV, POD and vortex identification algorithms for the study of unsteady turbulent swirling flows. *Meas. Sci. Technol.* 12 (9), 1422.
- Hemida, H., Baker, C., Gao, G., 2014. The calculation of train slipstreams using Large-Eddy Simulation. *Proc. Inst. Mech. Eng. - Part F J. Rail Rapid Transit* 228 (1), 25–36.
- Huang, S., Hemida, H., Yang, M., 2016. Numerical calculation of the slipstream generated by a crh2 high-speed train. *Proc. Inst. Mech. Eng. - Part F J. Rail Rapid Transit* 230 (1), 103–116.
- Jönsson, M., Wagner, C., Loose, S., 2014. Particle image velocimetry of the underfloor flow for generic high-speed train models in a water towing tank. *Proc. Inst. Mech. Eng. - Part F J. Rail Rapid Transit* 228 (2), 194–209.
- Mizushima, F., Takakura, H., Kurita, T., Kato, C., Iida, A., 2007. Experimental investigation of aerodynamic noise generated by a train-car gap. *J. Fluid Sci. Technol.* 2 (2), 464–479.
- Muld, T.W., Efraimsson, G., Henningson, D.S., 2012. Flow structures around a high-speed train extracted using proper orthogonal decomposition and dynamic mode decomposition. *Comput. Fluids* 57, 87–97.
- Muld, T.W., Efraimsson, G., Henningson, D.S., 2014. Wake characteristics of high-speed trains with different lengths. *Proc. Inst. Mech. Eng. - Part F J. Rail Rapid Transit* 228 (4), 333–342.
- Paz, C., Suárez, E., Gil, C., 2017. Numerical methodology for evaluating the effect of sleepers in the underbody flow of a high-speed train. *J. Wind Eng. Ind. Aerod.* 167, 140–147.
- Pombo, J., Ambrósio, J., Pereira, M., Rauter, F., Collina, A., Facchinetti, A., 2009. Influence of the aerodynamic forces on the pantograph–catenary system for high-speed trains. *Veh. Syst. Dyn.* 47 (11), 1327–1347.
- Quinn, A.D., Hayward, M., Baker, C.J., Schmid, F., Priest, J.A., Powrie, W., 2010. A full-scale experimental and modelling study of ballast flight under high-speed trains. *Proc. Inst. Mech. Eng. - Part F J. Rail Rapid Transit* 224 (2), 61–74.
- Raghunathan, R.S., Kim, H.-D., Setoguchi, T., 2002. Aerodynamics of high-speed railway train. *Prog. Aero. Sci.* 38 (6), 469–514.
- Railway applications, 2009. Aerodynamics part 4: requirements and test procedures for aerodynamics on open track cen en 14067-4.
- Railway applications, 2011. Aerodynamics part 4: requirements and test procedures for aerodynamics on open track cen en 14067-4.
- Railway applications, 2013. Aerodynamics part 4: requirements and test procedures for aerodynamics on open track cen en 14067-4.
- Soper, D., Baker, C., Jackson, A., Milne, D., Le Pen, L., Watson, G., Powrie, W., 2017a. Full scale measurements of train underbody flows and track forces. *J. Wind Eng. Ind. Aerod.* 169, 251–264.
- Soper, D., Flynn, D., Baker, C., Jackson, A., Hemida, H., 2017b. A comparative study of methods to simulate aerodynamic flow beneath a high-speed train. *Proc. Inst. Mech. Eng. - Part F J. Rail Rapid Transit*, 0954409717734090.
- Spalart, P.R., 2009. Detached-eddy simulation. *Annu. Rev. Fluid Mech.* 41, 181–202.
- DIN Standards Committee Railway/Normenausschuss Fahrweg und Schienenfahrzeuge (FSF), 2014. <http://www.fsf.din.de>.
- Wang, S., Bell, J.R., Burton, D., Herbst, A.H., Sheridan, J., Thompson, M.C., 2017. The performance of different turbulence models (URANS, SAS and DES) for predicting high-speed train slipstream. *J. Wind Eng. Ind. Aerod.* 165, 46–57.
- Wang, S., Burton, D., Herbst, A., Sheridan, J., Thompson, M.C., 2018a. The effect of bogies on high-speed train slipstream and wake. *J. Fluid Struct.* 83, 471–489.
- Wang, S., Burton, D., Herbst, A.H., Sheridan, J., Thompson, M.C., 2018b. The effect of the ground condition on high-speed train slipstream. *J. Wind Eng. Ind. Aerod.* 172, 230–243.
- Zhang, J., Li, J.-j., Tian, H.-q., Gao, G.-j., Sheridan, J., 2016. Impact of ground and wheel boundary conditions on numerical simulation of the high-speed train aerodynamic performance. *J. Fluid Struct.* 61, 249–261.